

Deep Frequency-Aware Functional Maps for Robust Shape Matching

Feifan Luo^{2*}, Qinsong Li^{1*}, Ling Hu⁴, Haibo Wang¹, Xinru Liu¹, Shengjun Liu^{1†}, Hongyang Chen^{2, 3†}

¹ Central South University, China

² Zhejiang University, China

³ Zhejiang Lab, China

⁴ Hunan First Normal University, China

Abstract

Deep functional map frameworks are widely employed for 3D shape matching. However, most existing deep functional map methods cannot adaptively capture important frequency information for functional map estimation in specific matching scenarios, i.e., lacking frequency awareness, resulting in poor performance when dealing with large deformable shape matching. To this end, we propose a novel unsupervised learning-based framework called Deep Frequency-Aware Functional Maps, which can gracefully cope with various shape matching scenarios. We first introduce a general constraint called Spectral Filter Operator Preservation to compute desirable functional maps, where the spectral filter operator encodes informative frequency information and can promote frequency awareness for deep functional map frameworks by learning a set of filter functions. Then, we directly utilize the proposed constraint as a loss function to supervise functional maps, pointwise maps, and filter functions simultaneously, where the filter functions are derived from the orthonormal Jacobi basis, and the coefficients of the basis are learnable parameters. Finally, we develop an effective refinement strategy to improve the final pointwise map, which incorporates our constraint and learned filter functions, leading to more robust and accurate correspondences during the inference process. Extensive experimental results on various datasets demonstrate that our approach outperforms the existing state-of-the-art methods, especially in challenging settings like datasets with non-isometric deformation and inconsistent topology.

1. Introduction

Nonrigid shape matching is a classic problem in shape analysis and related fields, aiming to establish a meaningful

*Equal contribution.

†Corresponding authors: shjliu.cg@csu.edu.cn (Shengjun Liu), hongyang@zhejianglab.com (Hongyang Chen).

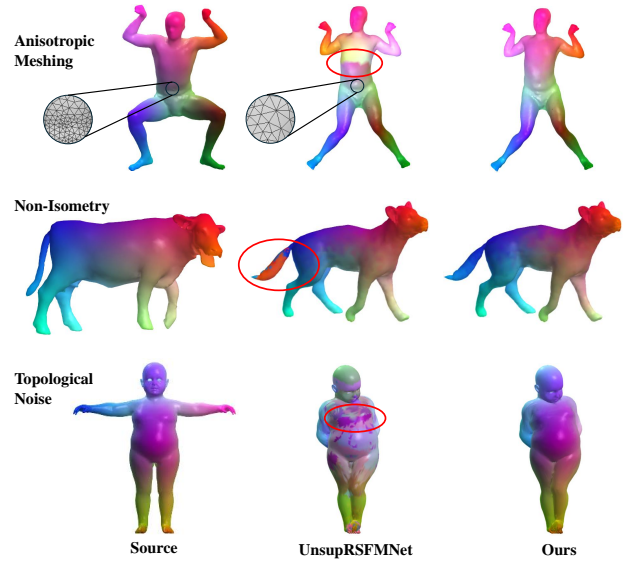


Figure 1. We propose a novel unsupervised spectral shape matching approach that is more robust than UnsupRSFMNet [6] across a broad range of challenging settings: shape matching with anisotropic meshing, shape matching of non-isometric shape pairs, shape matching with topological noise.

pointwise map or correspondence between shapes. It can be used in a variety of downstream tasks, such as deformation transfer [52], interpolation between shapes [15], and statistical shape analysis [4], among others.

Recently, researchers have developed numerous methods for shape correspondence. The functional maps [41] are one of the most influential frameworks due to their flexibility and efficient representation, aiming to transfer the functions between shapes and allowing for efficient optimization and interconversions with the pointwise map. The following works [10, 13, 20, 21, 31, 36, 38, 40, 46] have improved the functional map framework by introducing various informative preservation constraints or other technologies.

Unlike the functional map-based methods that utilize

handcrafted features, i.e., descriptor functions, the seminal work FMNet (also known as the deep functional maps) [30] was the first to use the learned features from shapes as the optimal descriptors to produce desired functional maps, which significantly enhanced the learning process as elegant geometric priors were considered. After that, numerous learning-based approaches were proposed for non-rigid 3D shape matching, such as supervised [9, 51], semi-supervised [50], and unsupervised methods [18, 47], as well as full shape correspondence [32, 55] and partial shape correspondence [1, 6, 22], among others. Although existing deep functional map methods have made significant advances, to the best of our knowledge, they lack frequency awareness, since different frequency information is treated the same in functional map computation, easily resulting in the important frequency information that positively affects the matching performance being ignored while unimportant frequency information is retained, leading to inadequate performance while handling large deformable matches.

Motivated by the above discussions, in this work, we first introduce a novel general constraint called Spectral Filter Operator Preservation with rigorous theoretical assurance, where the frequency information in the spectral filter operators is required to be preserved in functional map computing. Significantly, the spectral filter operator can be flexibly generated in a data-driven manner by adjusting a set of filter functions, which implies our constraint can adaptably maintain significant frequency information for calculating functional maps, contributing to acquiring more desirable correspondences in specific matching scenarios. With this foundation, we develop a novel learning-based framework called Deep Frequency-Aware Functional Maps (Deep FAFM for short) for shape matching by using our constraint as a novel unsupervised loss function to jointly optimize the pointwise maps, functional maps and a set of filter functions, where the filter functions are derived from the orthonormal Jacobi basis. This strategy allows for the simultaneous optimization of functional maps and pointwise maps and facilitates the learning of a collection of enhanced filters that adaptively focus on multi-resolution frequency features for a given deformable shape matching. Finally, we utilize our constraint and learned filter functions as a fast refinement technique to generate more accurate and robust results at inference time. Our main contributions are summarised as follows:

- We propose a novel general constraint called spectral filter operator for determining the functional maps, where the filter functions can be optimized for a specific task.
- Based on the proposed constraint, we design a Deep Frequency-Aware Functional Maps architecture for shape matching that allows us to obtain accurate and robust correspondences.
- We experimentally demonstrate that our method achieves

significant improvements in correspondence quality across a range of shape matching scenarios, especially in highly challenging non-isometric and inconsistent topology settings.

2. Related work

We refer readers to the survey [48] for an in-depth view of shape correspondence. Below we review the methods most related to ours.

2.1. Axiomatic functional map methods

Axiomatic shape matching methods are usually based on certain geometric assumptions and correspondence criteria that are defined as an optimization objective function. Establishing correspondences between shapes as in [7, 29, 34, 54], or introducing the correspondence distortion metric using pairwise descriptors of shapes like [59, 61], neither ignores the continuity in the map computation nor addresses the constituted optimization objective function, which is a nonconvex, NP-hard quadratic assignment problem. In contrast, the functional map [41] framework encodes the pointwise map as a low-dimensional and compact matrix, which can be efficiently optimized [41] for solving non-rigid shape matching problems and has been extended significantly in follow-up works [10, 16, 17, 20, 21, 23, 24, 31, 36, 38, 40, 42–44, 46]. Among them, incorporating more robust function or map constraints into functional maps to achieve more accurate and robust correspondence is the most common choice, such as LBOs commutativity [41], descriptor preservation [40], orientation preservation [10, 42], heat kernel preservation [58], wavelets preservation [21], smoothness pointwise mapping preservation [36], etc.

Different from the above methods, we propose a novel and powerful constraint that can selectively preserve important frequency information for functional map estimation in a learning manner. Moreover, we demonstrate that heat kernel preservation [58], ZoomOut [43], and wavelets preservation [21] are our special cases by using different functions to denote filter functions.

2.2. Deep functional map methods

In contrast to axiomatic functional map methods that are heavily dependent on the quality of the initial correspondences or descriptors, deep functional map methods attempt to avoid this limitation by learning features directly from training data as optimal descriptors. The pioneering work FMNet [30] used the SHOT descriptor [49] as input, optimizing it through residual multilayer perceptron (MLP) layers.

UnsupFMNet [18] introduced an unsupervised loss function by minimizing pairwise geodesic distance distortion, leading to comparable results with FMNet. In order to

avoid the time-consuming computation of geodesic distance, *Ayguen et al.* [3] replaced it with a computationally efficient heat kernel in UnsupFMNet [18]. All of the above works constrain the pointwise map as part of the loss functions, and an alternative strategy is to directly constrain the functional map [47, 50], including bijection, orthogonality, and commutativity with the LBOs. After that, researchers focused on feature extraction and functional map optimization modules.

GeomFMNet [9] directly extracted shape features from the shape vertex coordinates through KPConv [57], optimizing the functional map with a quadratic regular term by solving multiple linear systems. DiffusionNet [51], known as the state-of-the-art feature extractor capable of extracting discretization-resistant and orientation-aware shape features, serves as the basis for most of the follow-up work, such as [1, 5, 6, 11, 12, 22, 28, 55]. *Donati et al.* [12] introduced the complex functional map [11] into the deep functional map framework to tackle symmetry issues in shape matching but achieving poor performance in large distorted scenarios. AttentiveFMaps [28] combined functional maps of different spectral resolutions by introducing a spectral attention mechanism, however, it focuses on spectral resolution rather than frequency information. RFMNet [22] proposed a novel approach for functional map optimization with wavelets preservation [21], but failing to learn more flexible and expressive wavelet to better suit the dataset and task at hand. *Cao et al.* [6] developed a novel learning-based approach for robust shape matching and achieved superiority under different settings. However, this approach heavily relied on a refinement strategy called test-time adaptation to promote matching performance. Additionally, we show that the proposed coupling loss function in [6] is a special case of our unsupervised loss.

Despite the rapid progress of deep functional map methods, extracting beneficial frequency information in a learning manner to achieve desirable properties in functional map estimation remains neglected. To bridge this gap, we propose a novel unsupervised learning-based architecture that achieves state-of-the-art performance in diverse challenging settings by leveraging our powerful and flexible constraints.

3. Background and Notation

Given a pair of non-rigid shapes denoted as \mathcal{M} and \mathcal{N} respectively, let a pointwise map $T : \mathcal{M} \rightarrow \mathcal{N}$ between them, then the corresponding functional map T_F is a linear transformation taking functions on \mathcal{N} to functions on \mathcal{M} . Namely, given a function $g \in \mathcal{L}^2(\mathcal{N})$, we define its map $f \in \mathcal{L}^2(\mathcal{M})$ satisfying $f = T_F(g) = g \circ T$. If we use the truncated eigenfunctions (usually the first k) $\{\phi_i^{\mathcal{M}}\}_{i \geq 0}$ and $\{\phi_j^{\mathcal{N}}\}_{j \geq 0}$ of the Laplace-Beltrami operators (LBOs) defined in each shape as the basis to represent the

functions, then the functional map T_F can be expressed as a $k \times k$ matrix \mathbf{C} , which could transfer the basis coefficients of the functions between the shapes.

In discrete settings, the shape \mathcal{M} and shape \mathcal{N} are typically represented as two triangle meshes, with $n_{\mathcal{M}}$ and $n_{\mathcal{N}}$ vertices respectively. Then the function f in $\mathcal{L}^2(\mathcal{N})$ is discretized to a vector $\mathbf{f} \in \mathbb{R}^{n_{\mathcal{N}} \times 1}$. According to the standard cotangent weight scheme [39], the Laplace-Beltrami operators (LBOs) defined on them can be represented as Laplacian matrices $\mathbf{L}_{\mathcal{M}}$ and $\mathbf{L}_{\mathcal{N}}$, where $\mathbf{L}_{\mathcal{M}} = \mathbf{A}_{\mathcal{M}}^{-1} \mathbf{B}_{\mathcal{M}} \in \mathbb{R}^{n_{\mathcal{M}} \times n_{\mathcal{M}}}$, $\mathbf{L}_{\mathcal{N}} = \mathbf{A}_{\mathcal{N}}^{-1} \mathbf{B}_{\mathcal{N}} \in \mathbb{R}^{n_{\mathcal{N}} \times n_{\mathcal{N}}}$ respectively, here the matrix \mathbf{A} is the diagonal matrix of lumped area elements and \mathbf{B} is the cotangent weight matrix. We make use of the basis consisting of the first k eigenfunctions of the Laplacian matrix and encode it in a matrix $\Phi_{\mathcal{M}} = [\phi_1^{\mathcal{M}}, \phi_2^{\mathcal{M}}, \dots, \phi_k^{\mathcal{M}}] \in \mathbb{R}^{M \times k}$ having the eigenfunctions as its columns. We also encode the first k eigenvalues of the Laplacian matrix as a diagonal matrix $\Lambda^{\mathcal{M}} = \text{diag}\{\lambda_1, \lambda_2, \dots, \lambda_k\} \in \mathbb{R}^{k \times k}$ with the eigenvalues as its diagonal elements.

Now the pointwise map $T : \mathcal{M} \rightarrow \mathcal{N}$ can also be expressed as a matrix $\Pi_{\mathcal{M}\mathcal{N}} \in \mathbb{R}^{n_{\mathcal{M}} \times n_{\mathcal{N}}}$, s.t. $\Pi_{\mathcal{M}\mathcal{N}}(i, j) = 1$, if $T(i) = j$ and 0 otherwise, where i and j denote the vertex indices of shapes \mathcal{M} and \mathcal{N} , respectively. Now, the map image \mathbf{f} of \mathbf{g} can be represented as $\mathbf{f} = \Pi_{\mathcal{M}\mathcal{N}} \mathbf{g}$. In matrix notation, $\mathbf{C}_{\mathcal{N}\mathcal{M}}$ is given by the projection of $\Pi_{\mathcal{M}\mathcal{N}} \in \mathbb{R}^{n_{\mathcal{M}} \times n_{\mathcal{N}}}$ onto the corresponding functional basis, i.e., $\mathbf{C}_{\mathcal{N}\mathcal{M}} = \Phi_{\mathcal{M}}^{\dagger} \Pi_{\mathcal{M}\mathcal{N}} \Phi_{\mathcal{N}}$, where $\Phi_{\mathcal{M}}^{\dagger} = \Phi_{\mathcal{M}}^T \mathbf{A}_{\mathcal{M}}$ is the Moore-Penrose pseudo-inverse of $\Phi_{\mathcal{M}}$.

Generally, the computation of the functional map $\mathbf{C}_{\mathcal{N}\mathcal{M}}$ mainly resorts to the constraints of descriptor preservation. Namely, given d -dimensional features $\mathbf{D}_{\mathcal{M}} \in \mathbb{R}^{n_{\mathcal{M}} \times d}$ and $\mathbf{D}_{\mathcal{N}} \in \mathbb{R}^{n_{\mathcal{N}} \times d}$ computed on each shape, they will be approximately preserved by the mapping T . As the functional map $\mathbf{C}_{\mathcal{N}\mathcal{M}}$ transfers the basis coefficients of the functions between the shapes, this allows the functional map $\mathbf{C}_{\mathcal{N}\mathcal{M}}$ satisfying the system of linear equations $\mathbf{C}_{\mathcal{N}\mathcal{M}} \Phi_{\mathcal{M}}^{\dagger} \mathbf{D}_{\mathcal{M}} = \Phi_{\mathcal{N}}^{\dagger} \mathbf{D}_{\mathcal{N}}$. In practice, this equation often couples with some penalization terms, i.e.,

$$\mathbf{C}_{\mathcal{N}\mathcal{M}} = \arg \min_{\mathbf{C}_{\mathcal{N}\mathcal{M}}} \left\| \Phi_{\mathcal{M}}^{\dagger} \mathbf{D}_{\mathcal{M}} - \mathbf{C}_{\mathcal{N}\mathcal{M}} \Phi_{\mathcal{N}}^{\dagger} \mathbf{D}_{\mathcal{N}} \right\|_{\text{F}}^2 + \lambda E_{\text{reg}}(\mathbf{C}_{\mathcal{N}\mathcal{M}}), \quad (1)$$

where $\|\cdot\|_{\text{F}}$ denotes Frobenius norm.

As a last step, the estimated map $\mathbf{C}_{\mathcal{N}\mathcal{M}}$ can be converted to a point-to-point map commonly by nearest neighbor search between the aligned spectral embeddings, namely, $\Pi_{\mathcal{M}\mathcal{N}} = \text{NNsearch}(\Phi_{\mathcal{N}} \mathbf{C}_{\mathcal{N}\mathcal{M}}^T, \Phi_{\mathcal{M}})$.

4. Functional maps with spectral filter operator preservation

While suitable preservation constraints play an important role in the functional map framework, explorations that make the pointwise maps maintain frequency awareness

are rarely explored, i.e., adaptively capturing important frequency information for functional map estimation. To fill this gap, we first introduce a novel constraint called Spectral Filter Operator Preservation with rigorous theoretical guarantees and show how to compute the functional map with the proposed preservation. More importantly, the filter functions in this preservation can be represented by arbitrary functions, which means our constraint can flexibly emphasize favorable frequency information by constructing a set of filter functions, laying the foundation for the next learning-based framework. Finally, we show that heat kernel preservation [58], ZoomOut [43], and wavelets preservation [21] are our special cases.

4.1. Spectral Filter Operator Preservation

In order to encode the informative frequency information, we first define a spectral filter operator on the shape \mathcal{N} as $R : \mathcal{L}^2(\mathcal{N}) \rightarrow \mathcal{L}^2(\mathcal{N})$, which is used to enhance or suppress a certain part of the frequency of the input functions (or signals). From a spectral signal processing perspective, as the ordered eigenfunctions and the eigenvalues of the LBOs analogously play the role of Fourier basis and frequency, we can arbitrarily filter any function by virtue of designing appropriate spectral filters. For convenience, we directly discuss them in a discrete setting.

Given a function \mathbf{f} defined on the shape \mathcal{N} , and a filter function $h(\lambda)$, the spectral filter operator \mathbf{R} (can also be represented as a matrix) on the signal \mathbf{f} will be expressed as

$$\mathbf{R}\mathbf{f} = \Phi h(\Lambda)\Phi^\dagger \mathbf{f}, \quad (2)$$

where $h(\Lambda) = \text{diag}\{h(\lambda_1), h(\lambda_2), \dots, h(\lambda_k)\}$. It means we adjust the Fourier coefficients of \mathbf{f} (i.e., $\Phi^\dagger \mathbf{f}$) by means of $h(\Lambda)$ (i.e., $h(\Lambda)\Phi^\dagger \mathbf{f}$) and then get the filtered functions by making inverse Fourier transform.

Obviously, the choice of the filter function h plays a key role in the spectral filter operator. Actually, plenty of functions have been used as filters in the shape analysis field for different tasks, such as heat diffusion [53], wave kernel [2], or any others, aiming to extract different frequency information of signals. Perhaps the most desirable way to address this issue is data-driven, and designing learnable preservation is one part of our work's motivation.

Remark 4.1. *If the pointwise map $T : \mathcal{M} \rightarrow \mathcal{N}$ be isometric, given a function $f \in \mathcal{L}^2(\mathcal{N})$, let $R_{\mathcal{M}}$ and $R_{\mathcal{N}}$ respectively denote the spectral filter operator on the shape \mathcal{M} and \mathcal{N} , which have the same filter function $h(\lambda)$ acting on their corresponding eigenfunctions and eigenvalues of their LBOs, then these spectral filter operators will be preserved by the corresponding functional map, i.e.,*

$$T_F(R_{\mathcal{N}}f) = R_{\mathcal{M}}T_F(f). \quad (3)$$

and specially in the discrete setting, we have

$$\mathbf{C}_{\mathcal{N}\mathcal{M}}h(\Lambda_{\mathcal{N}})\Phi_{\mathcal{N}}^\dagger = h(\Lambda_{\mathcal{M}})\Phi_{\mathcal{M}}^\dagger\Pi_{\mathcal{M}\mathcal{N}}. \quad (4)$$

Proof. The Eq.(3) is true as the spectral filter operators are still intrinsic as analyzed above. In discrete settings, the above equation can be presented as matrix operations. Note that the function map $\mathbf{C}_{\mathcal{N}\mathcal{M}}$ transfers the coefficients w.r.t the basis, we get the coefficient matrix of $T_F(R_{\mathcal{N}}\mathbf{f})$ be $\mathbf{C}_{\mathcal{N}\mathcal{M}}h(\Lambda_{\mathcal{N}})\Phi_{\mathcal{N}}^\dagger\mathbf{f}$. As $T_F(f)$ can be represented as the vector $\Pi_{\mathcal{M}\mathcal{N}}\mathbf{f}$, its coefficients are given as $\Phi_{\mathcal{M}}^\dagger\Pi_{\mathcal{M}\mathcal{N}}\mathbf{f}$, and the coefficient matrix of $R_{\mathcal{M}}T_F(f)$ is $h(\Lambda_{\mathcal{M}})\Phi_{\mathcal{M}}^\dagger\Pi_{\mathcal{M}\mathcal{N}}\mathbf{f}$. According to the operator preservation constraint, as shown in Eq.(3), and note that the functions being equal means their coefficients w.r.t the same basis are identical, we state that

$$\mathbf{C}_{\mathcal{N}\mathcal{M}}h(\Lambda_{\mathcal{N}})\Phi_{\mathcal{N}}^\dagger\mathbf{f} = h(\Lambda_{\mathcal{M}})\Phi_{\mathcal{M}}^\dagger\Pi_{\mathcal{M}\mathcal{N}}\mathbf{f}. \quad (5)$$

Since the Eq.(5) is true for any function \mathbf{f} , we finally conclude that the map with spectral filter operator preservation equals to require Eq. (4). \square

Since $\Phi_{\mathcal{N}}^\dagger\Phi_{\mathcal{N}} = \mathbf{I}$, by multiplying the matrix $\Phi_{\mathcal{N}}$ to the right on both sides of the Eq.(4), we deduce the spectral filter operator commutativity, given by

$$\mathbf{C}_{\mathcal{N}\mathcal{M}}h(\Lambda_{\mathcal{N}}) = h(\Lambda_{\mathcal{M}})\mathbf{C}_{\mathcal{N}\mathcal{M}}^\Pi, \quad (6)$$

where $\mathbf{C}_{\mathcal{N}\mathcal{M}}^\Pi = \Phi_{\mathcal{M}}^\dagger\Pi_{\mathcal{M}\mathcal{N}}\Phi_{\mathcal{N}}$ recovers from the pointwise map $\Pi_{\mathcal{M}\mathcal{N}}$. From the above observation, our spectral filter operator preservation can be considered as using filter functions that acts on the spectrum and exchanging them with functional maps. There are two main benefits to our approach: (1) Our preservation ensures that the optimized functional map is related to underlying pointwise maps, which implies that we can obtain a *proper* functional map [45] by solving Eq. (6), leading to a more accurate pointwise map. (2) Our constraint enables us to flexibly encode desired frequency information by adjusting diagonal filter functions, hence promoting functional and pointwise maps for specific matching tasks.

In the next section, we show how to use this important constraint to compute the functional map and the pointwise map.

4.2. Compute maps with Spectral Filter Operator Preservation

One single spectral filter operator preservation in Eq.(4) may not be able to comprehensively encode the frequency features of the maps, since one operator allows to process certain frequency band information only. To address this issue, we use the preservation of multiple spectral filter operators as the constraint to compute the functional map $\mathbf{C}_{\mathcal{N}\mathcal{M}}$ and the underlying pointwise map $\Pi_{\mathcal{M}\mathcal{N}}$.

Given a set of filter functions $\{h_s(\lambda)\}_{s=1}^S$, according to Eq.(4), we eventually formulate our strategy of computing

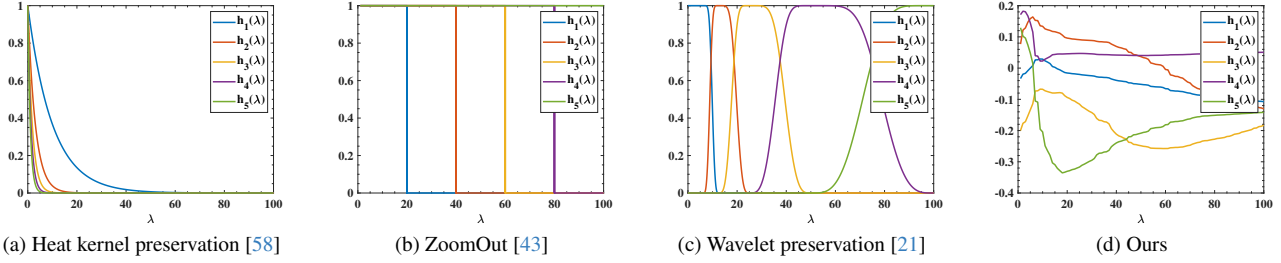


Figure 2. The filter functions of different methods. (a) The filter functions in heat kernel preservation are low-pass, focusing on low frequency information only. (b) The filter functions of ZoomOut are upsampled ideal filters, using to upsample resolutions of eigenfunctions (c) Meyer wavelet functions consist of a low-pass and a set of band-pass in wavelet preservation are tight frames strictly (d) Our learned filter functions are optimized on non-isometric datasets SMALr.

the maps as the following problem

$$\begin{aligned} \min_{\Pi_{\mathcal{M}\mathcal{N}}, \mathbf{C}_{\mathcal{N}\mathcal{M}}} & \left\| \mathbf{C}_{\mathcal{N}\mathcal{M}} H(\Lambda_{\mathcal{N}}) - H(\Lambda_{\mathcal{M}}) * \mathbf{C}_{\mathcal{N}\mathcal{M}}^{\Pi} \right\|_{\text{F}}^2, \\ \text{s.t.} & \quad \Pi_{\mathcal{M}\mathcal{N}} \mathbf{1} = \mathbf{1}, \Pi_{\mathcal{M}\mathcal{N}}^{\text{T}} \mathbf{1} \leq \mathbf{1}, \end{aligned} \quad (7)$$

where the filter function matrix $H(\Lambda) = [h_1(\Lambda) \parallel h_2(\Lambda) \parallel \dots \parallel h_S(\Lambda)] \in \mathbb{R}^{k \times (S \cdot k)}$, \parallel denotes matrix connection, and $H(\Lambda_{\mathcal{M}}) * \mathbf{C}_{\mathcal{N}\mathcal{M}}^{\Pi} = [h_1(\Lambda_{\mathcal{M}}) \mathbf{C}_{\mathcal{N}\mathcal{M}}^{\Pi} \parallel \dots \parallel h_S(\Lambda_{\mathcal{M}}) \mathbf{C}_{\mathcal{N}\mathcal{M}}^{\Pi}]$.

Given the pointwise map matrix $\Pi_{\mathcal{M}\mathcal{N}}$, then the Eq.(7) is transformed to the following problem

$$\mathbf{C}_{\mathcal{N}\mathcal{M}}^* = \min_{\mathbf{C}_{\mathcal{N}\mathcal{M}}} \left\| \mathbf{C}_{\mathcal{N}\mathcal{M}} H(\Lambda_{\mathcal{N}}) - H(\Lambda_{\mathcal{M}}) * \mathbf{C}_{\mathcal{N}\mathcal{M}}^{\Pi} \right\|_{\text{F}}^2. \quad (8)$$

Next, we efficiently compute $\mathbf{C}_{\mathcal{N}\mathcal{M}}^*$ via the following important observation.

Remark 4.2. *If the set of filter functions $\{h_s(\lambda)\}_{s=1}^S$ satisfy the condition that $\sum_s h_s^2(\lambda) \neq 0, \forall \lambda$, then the functional map $\mathbf{C}_{\mathcal{N}\mathcal{M}}$ in Eq.(8) can be obtained via*

$$\mathbf{C}_{\mathcal{N}\mathcal{M}}^* = \left(\sum_s h_s(\Lambda_{\mathcal{M}}) \mathbf{C}_{\mathcal{N}\mathcal{M}}^{\Pi} h_s(\Lambda_{\mathcal{N}}) \right) (G^{-1}(\Lambda_{\mathcal{N}})). \quad (9)$$

where $G(\Lambda_{\mathcal{N}}) = \sum_s h_s^2(\Lambda_{\mathcal{N}})$.

Proof. See Appendix A. \square

Interestingly, Eq (9) is consistent with the intuition of signal denoising, which means that we actually use multiple filters to refine the coarse functional map $\mathbf{C}_{\mathcal{N}\mathcal{M}}^{\Pi}$. Additionally, we can obtain the pointwise map through the nearest neighbor search, and even update the functional maps and pointwise map alternatively [41].

4.3. Relation to other techniques

In this section, we highlight that the similar works heat kernel preservation [58], ZoomOut [43], and wavelets preservation [21] are actually special cases of our framework.

Heat Kernel Preservation. Heat kernel preservation [58] introduced an optimization problem by using positive-definite heat kernel matrices to construct pairwise descriptors, where the functional maps are seen as a low-pass approximation of the permutation matrix in the truncated Laplacian eigenfunctions, and the alternating heat diffusion between shapes can be interpreted as applying a set of low-pass filters to the functional map matrix, i.e., setting $h(\lambda) = e^{-t\lambda}$ in Eq. (9), see Fig. 2 (a). Nevertheless, the heat kernel cannot encode informative features since it overlooks band-pass or high-pass frequency information.

ZoomOut. ZoomOut introduced an iterative spectral upsampling technique to align the functional maps and pointwise map from low to high frequencies, which can be considered as using a set of upsampled ideal filters to represent $\{h_s(\lambda)\}_{s=1}^S$ in Eq. (7). For instance,

setting $h_1(\Lambda) = \text{diag}\{\overbrace{1, \dots, 1}^{k_1}, 0, \dots, 0\}$,

$h_2(\Lambda) = \text{diag}\{\overbrace{1, 1, \dots, 1}^{k_2}, 0, \dots, 0\}, \dots, h_S(\Lambda) = \text{diag}\{1, 1, \dots, 1, 1, \dots, 1\}$, where $k_1 < k_2 < \dots < k$, see Fig. 2 (b). In fact, a set of upsampled ideal filters are used to partition the eigenfunction matrix

$\Phi_{\mathcal{M}} \in \mathbb{R}^{M \times k}$ into upsampled spectral resolutions sets $\{\Phi_{\mathcal{M},1} \in \mathbb{R}^{M \times k_1}, \Phi_{\mathcal{M},2} \in \mathbb{R}^{M \times k_2}, \dots, \Phi_{\mathcal{M},S}\}$, where $\Phi_{\mathcal{M},1}$ consists of the first k_1 columns of the matrix $\Phi_{\mathcal{M}}$, $\Phi_{\mathcal{M},S} = \Phi_{\mathcal{M}}$. By using those partitions $\{\Phi_{\mathcal{M},1}, \Phi_{\mathcal{M},2}, \dots, \Phi_{\mathcal{M},S}\}$ to recover functional maps iteratively, then we construct ZoomOut. However, ZoomOut cannot enhance or suppress the frequency information softly since the value of the upsampled ideal filter is either 0 or 1, leading to loss of information easily.

Wavelet Preservation. Multiple spectral manifold wavelets in wavelet preservation [21] are required to be preserved at each scale correspondingly. When we specify our filter functions $\{h_s(\lambda)\}$ to be the multi-scale tight frame Meyer functions [27] (see Fig. 2 (c)), our work will degrade to the wavelet preservation [21]. However, wavelet

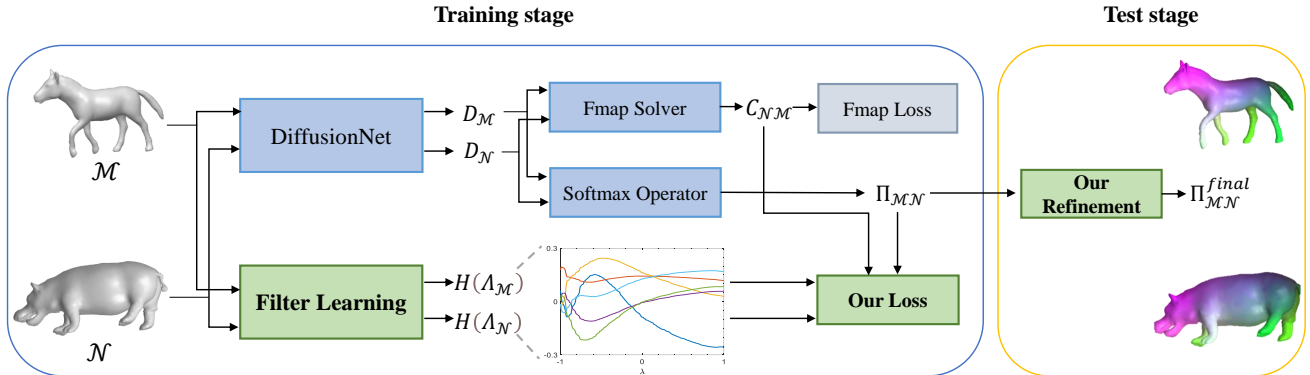


Figure 3. An overview of Deep FAFM. (1) Inputting a pair of shapes \mathcal{M} and \mathcal{N} to a trainable Siamese feature network to produce learned features $\mathbf{D}_{\mathcal{M}}$ and $\mathbf{D}_{\mathcal{N}}$ respectively. (2) Employing the filter learning layer to produce learned filter functions $H(\Lambda_{\mathcal{M}})$ and $H(\Lambda_{\mathcal{N}})$ respectively, i.e., Eq. (12). (3) Utilizing learned features to compute the differentiable pointwise map $\Pi_{\mathcal{M}\mathcal{N}}$ and functional map $C_{\mathcal{N}\mathcal{M}}$ by resorting to Softmax operator (Eq. (10)) and functional map solver (Eq. (1)) respectively. (4) A frequency awareness loss term (Eq. (13)) is used to supervise the functional map $C_{\mathcal{N}\mathcal{M}}$, pointwise map $\Pi_{\mathcal{M}\mathcal{N}}$, as well as $H(\Lambda_{\mathcal{M}})$ and $H(\Lambda_{\mathcal{N}})$. (5) Using our refinement technique (Eq. (9)) to refine a pointwise map $\Pi_{\mathcal{M}\mathcal{N}}$, resulting in a more accurate and robust final correspondence $\Pi_{\mathcal{M}\mathcal{N}}^{final}$ at the test stage.

functions in the preservation are unlearnable and analyze the fixed frequency features only.

From the above discussions, heat kernel preservation [58], ZoomOut [43] and wavelet preservation [21] are actually special cases of our constraint, which can be considered as using different functions that act on the spectrum and applying them to functional maps, i.e., heat kernel functions for heat kernel preservation, upsampled ideal filter functions for ZoomOut and wavelet functions [19] for wavelet preservation, respectively. Those preservation constraints can be harmonized into a general paradigm, i.e., Eq (7).

Moreover, the preservation constraints mentioned are not able to construct adaptable filter functions to extract frequency information for functional map estimation, which greatly limits their application. Instead, our constraint allows us to flexibly choose filter functions and even make them learnable, contributing to obtaining more desirable constraints to compute the maps. See Fig. 2 (d). Our filter functions are optimized for specific matching scenarios, encoding more suitable frequency features to promote the correspondence results.

In the next section, we will use the proposed constraint to construct a novel frequency-aware learning framework for shape matching.

5. Deep Frequency-Aware Functional Maps

Based on the aforementioned spectral filter operator preservation, we propose a novel and efficient unsupervised deep functional map architecture, called Deep Frequency-Aware Functional Maps (Deep FAFM). The overview of its pipeline is demonstrated in Fig. 3.

5.1. Learning input pointwise maps

Unlike the approaches [8, 13] that use the time-consuming Optimal Transport algorithm to compute the differentiable soft map $\Pi_{\mathcal{M}\mathcal{N}}$ after extracting the shape features, a common strategy[6, 15] adopts the efficient softmax operator to yield a soft correspondence matrix, i.e.,

$$\Pi_{\mathcal{M}\mathcal{N}} = \text{Softmax}(D_{\mathcal{M}}D_{\mathcal{N}}^T/\tau), \quad (10)$$

where the element at position (i, j) represents the probability of correspondence between the i -th point in \mathcal{M} and the j -th point in \mathcal{N} , and τ is the scaling factor to determine the softness of the correspondence matrix.

5.2. Filter parameterization

An important property is that our constraint can promote frequency awareness for functional map estimation by learning a set of filter functions. In this section, we provide an instance for parameterizing the filter functions.

Learnable filter functions. The core of our idea is to use a linear combination of a set of basis functions $\{g_l\}_{l=0}^L$ to represent each filter function and make all the representative coefficients learnable. Namely, let

$$h_s(\lambda) = \sum_l w_{sl}g_l(\lambda), s = 1, 2, \dots, S. \quad (11)$$

Encoding all representative coefficients of S filter functions as a matrix $W = (w_{sl}) \in \mathbb{R}^{L \times S}$, with each filter function's coefficients as a column.

Basis for filter functions. Various basis functions could be used to express our learnable filter functions. Here we choose the Jacobi basis to express them, as they have many

attractive properties such as orthogonality, excellent capacity of representation, recursive computation, and so on. In particular, the Jacobi basis has a very general form, with several orthogonal bases as their special cases, such as the Chebyshev basis and the Legendre basis.

Now, we express our filter functions based on a set of Jacobi bases $\{J_l^{a,b}(\lambda)\}_{l=0}^L$, i.e.,

$$h_s(\lambda) = \sum_l w_{sl} J_l^{a,b}(\lambda), \quad (12)$$

where a and b are also trainable parameters. For ease of reading, more details regarding the description of the Jacobi basis and how to integrate them into our network are shown in Appendix B.

5.3. Unsupervised loss

We propose a novel unsupervised loss called Frequency-Aware Loss to jointly supervise the functional map, the pointwise map, and filter functions training for our network by employing our preservation directly, i.e.,

$$L_{freq} = \|\mathbf{C}_{\mathcal{N}\mathcal{M}}^\Pi H(\Lambda_{\mathcal{N}}) - H(\Lambda_{\mathcal{M}}) * \mathbf{C}_{\mathcal{N}\mathcal{M}}^\Pi\|_{\mathbb{F}}^2, \quad (13)$$

where $\mathbf{C}_{\mathcal{N}\mathcal{M}}^\Pi = \Phi_{\mathcal{M}}^\dagger \Pi_{\mathcal{M}\mathcal{N}} \Phi_{\mathcal{N}}$ recovers from the soft pointwise map matrix $\Pi_{\mathcal{M}\mathcal{N}}$ via Eq. (10), $\mathbf{C}_{\mathcal{N}\mathcal{M}}$ is obtained by solving Eq. (1), and $H(\Lambda)$ is calculated by Eq. (12), respectively. Unlike most existing deep functional map methods that focus on predicting optimized functional maps alone, resulting in sub-optimal performance often, our loss ensures that the functional map is associated with a valid pointwise map and optimizes them simultaneously under different frequency channels. Moreover, our loss embeds parameterizable filter functions for frequency analysis, which can capture ideal spectral information effectively for obtaining frequency-aware functional and pointwise maps, leading to more accurate and robust correspondence results.

Interestingly, by setting $H(\Lambda) = \mathbf{I}, S = 1$, our loss is equivalent to the coupling loss introduced by *Cao et al.* [6], i.e.,

$$L_{co} = \|\mathbf{C}_{\mathcal{N}\mathcal{M}} - \Phi_{\mathcal{M}}^\dagger \Pi_{\mathcal{M}\mathcal{N}} \Phi_{\mathcal{N}}\|_{\mathbb{F}}^2, \quad (14)$$

which confirms that the coupling loss is a special case of ours. Nevertheless, the coupling loss is non-frequency awareness as it falls short in encoding instructive and significant frequency features adaptably. Conversely, our loss offers superior filtering flexibility and surpasses it.

In addition, the common structural functional map regularisation [43] is used to penalize the bijectivity and orthogonality of the functional maps, i.e.,

$$L_{fmap} = \theta_{bi} L_{bi} + \theta_{or} L_{or}, \quad (15)$$

where the bijectivity and orthogonality loss terms can be expressed as $L_{bi} = \|\mathbf{C}_{\mathcal{N}\mathcal{M}} \mathbf{C}_{\mathcal{M}\mathcal{N}} - \mathbf{I}\|_{\mathbb{F}}^2$ and $L_{or} = \|\mathbf{C}_{\mathcal{N}\mathcal{M}} \mathbf{C}_{\mathcal{N}\mathcal{M}}^\top - \mathbf{I}\|_{\mathbb{F}}^2$ respectively.

To handle non-isometric matching, we also use the smoothness penalty on the pointwise map, based on the Dirichlet energy of shape vertices, i.e.,

$$L_{sm} = \|\Pi_{\mathcal{M}\mathcal{N}} V_{\mathcal{N}}\|_{W_{\mathcal{N}}}^2, \quad (16)$$

where $W_{\mathcal{N}}$ is the cotangent weight matrix of shape \mathcal{N} . At last, our final loss is presented as the weighted combination of the above-stated loss functions,

$$L_{total} = \theta_{freq} L_{freq} + \theta_{fmap} L_{fmap} + \theta_{sm} L_{sm}. \quad (17)$$

Last but not least, we can change the direction of the pointwise map and functional map to build a bidirectional loss function, which can penalize them bidirectionally.

5.4. Pointwise maps computation during inference

To promote the accuracy and robustness of the final pointwise maps during the test stage, several post-processing techniques from the axiomatic functional map methods [13, 21, 43] are commonly employed by existing deep functional map approaches [12, 14, 22]. Unlike previous deep functional map methods that directly output the results without updating the parameters during inference, UnsupRSFM-Net [6] introduced a refinement strategy called test-time adaptation to adjust the parameters of the networks for each test pair individually via 15 backpropagation iterations, essentially, which is equivalent to training the networks on the test datasets. Meanwhile, its superior performance relies almost entirely on this extremely time-consuming refinement technique. Fortunately, our method, i.e., Eq. (9), explicitly models the relation between the functional maps, the pointwise maps and a set of filter functions, which serves as a natural refinement technique by using the learned filter functions to refine the functional maps.

During inference, we first directly obtain the pointwise map based on similarities of learned feature by using nearest neighbour search, i.e.,

$$\Pi_{\mathcal{M}\mathcal{N}} = NNsearch(D_{\mathcal{N}}, D_{\mathcal{M}}). \quad (18)$$

Note that the optimized filter functions $H(\Lambda_{\mathcal{M}})$ and $H(\Lambda_{\mathcal{N}})$ are supervised by frequency awareness loss term Eq. (13), so the filter functions obviously retain desirable frequency information and ignore the noise frequency information. Then, with the computed pointwise map matrix $\Pi_{\mathcal{M}\mathcal{N}}$, as well as the learned filter functions $H(\Lambda_{\mathcal{M}})$ and $H(\Lambda_{\mathcal{N}})$, we spontaneously obtain the more accurate and robust functional maps $\mathbf{C}_{\mathcal{N}\mathcal{M}}^*$ via Eq. (9).

Finally, the final pointwise map is acquired by using nearest neighbour search again, i.e., $\Pi_{\mathcal{M}\mathcal{N}}^{final} = NNsearch(\Phi_{\mathcal{N}} \mathbf{C}_{\mathcal{N}\mathcal{M}}^{*\top}, \Phi_{\mathcal{M}})$.

6. Experiments and results

6.1. Implementation

We use DiffusionNet as a feature extractor with its default settings, which uses 128-dimensional WKS [2] as input features and produces 256-dimensional learned features for the Deep FAFM network. We set the number of Jacobi basis orders $L = 8$, the number of channels of spectral filters $S = 6$, and the truncated eigensystems $k = 200$. For point-wise map and functional map computation, we set $\tau = 0.07$ in Eq. (10) and $\lambda = 100$ in Eq. (1) respectively, where the functional map is solved via the regularised functional map solver [43]. In terms of our unsupervised loss, we empirically set $\theta_{bi} = 1$ and $\theta_{or} = 1$ in Eq.(15), $\theta_{freq} = 1$ in Eq.(13) for near-isometric matching. In the context of non-isometric matching, the loss weight λ_{sm} for the smoothness penalty term is set to 5.0. For training, we use the Adam optimizer [26] with a learning rate of 0.001 for all learning parameters. Note that, we use the mean geodesic error [25] to evaluate shape correspondence accuracy, which is computed over all pairs and points in the dataset and normalized by the geodesic diameter of the source shape.

6.2. Baselines

We extensively compare our method with existing non-rigid shape matching methods, which we categorize as follows:

- *Axiomatic approaches*, including BCICP [42], ZoomOut [38], Smooth Shells [13], DiscreteOp [44], and MWP [21].
- *Unsupervised approaches*, including Deep Shells [14], DUO-FMNet [12], WTFMNet [33], AttentiveFMaps [28], RFMNet [22] and UnsupRSFMNet [6], where UnsupRSFMNet has dropped test-time-adaptation in the following experiments since it finds the optimal parameters during testing, which is an unfair comparison for other approaches. Moreover, we compare with UnsupRSFMNet in the same scenario by using the strategy of test-time-adaptation, and the results are summarized in Appendix C, which shows our better performance.

6.3. Results

Extensive experimental results on plenty of datasets including challenging ones such as non-isometric and noisy datasets are used to evaluate our method with several state-of-the-art shape correspondence methods. All results are multiplied by 100 for the sake of readability.

Near-isometric shape matching. We evaluate our method on the remeshed versions [42] of the standard benchmarks FAUST and SCAPE (F_r and S_r for short, respectively), which are more challenging than the original datasets. The FAUST consists of 100 human shapes, showing 10 different people in 10 different poses, and is split into

80/20 for training and testing. The SCAPE contains 71 human shapes, displaying the same person in different poses, is split into 51/20 for training and testing.

The results of these benchmarks are provided in Table 1, where our method is compared with current state-of-the-art axiomatic and unsupervised learning approaches. The results indicate that our method performs better than the previous state-of-the-art methods.

Table 1. Benchmark tests on remeshed FAUST, SCAPE, and the robustness evaluation on anisotropic remeshed FAUST, SCAPE, respectively. The numbers in the table are mean geodesic errors ($\times 100$). **Bold**: Best, Underline: Runner-up.

Train	F_r		S_r	
Test	F_r	F_a	S_r	S_a
Axiomatic Methods				
BCICP	6.1	8.5	11.0	14.0
ZoomOut	6.1	8.7	7.5	15.0
SmoothShells	2.5	5.4	4.7	5.0
DiscreteOp	5.6	6.2	13.1	14.6
MWP	3.1	8.2	4.1	8.7
Unsupervised Methods				
Deep Shells	1.7	12.0	2.5	10.0
DUO-FMNet	2.5	3.0	2.6	2.7
WTFM	2.6	4.3	3.1	4.8
AttentiveFMaps	1.9	<u>2.4</u>	2.2	<u>2.3</u>
RFMNet	1.7	3.6	2.1	3.9
UnsupRSFMNet	<u>1.6</u>	2.5	<u>1.9</u>	5.5
Ours	1.6	2.0	1.9	1.9

Matching with anisotropic meshing. To evaluate the robustness on different discretizations, we train networks on remeshed datasets and test them on anisotropic remeshed versions (denoted F_a and S_a, respectively), which have different mesh connectivity to the original datasets.

Based on the results presented in Table 1, we can observe that our method demonstrates greater resilience to changes in triangulation compared to existing state-of-the-art methods [6, 22]. These methods, which suffer significant performance declines during testing, tend to overfit mesh connectivity, resulting in inaccurate predictions. In contrast, our method exhibits stronger robustness to varying mesh connectivity and consistently surpasses the current state of the art.

Cross-dataset Generalization. The performance of generalization across datasets has been the focus of attention, and here, we set up four sets of experiments to evaluate the performance of our method in generalization across datasets, i.e., training on F_r and testing on S_r and S_a, and vice versa. As shown in Table 2, the results demonstrate our approach achieves comparable performance with state-of-the-art in most settings. Nevertheless, the existing cutting-edge approach [6] suffers from huge performance drops

when tested on the cross-dataset generalisation datasets, which demonstrates substantially its inadequate generalization ability compared to existing learning-based methods, and our method is much more robust than it.

Table 2. Cross-dataset generalization evaluation on anisotropic remeshed FAUST, SCAPE, respectively. The numbers in the table are mean geodesic errors ($\times 100$). **Bold**: Best, Underline: Runner-up.

Train	F _r		S _r	
Test	S _r	S _a	F _r	F _a
Axiomatic Methods				
BCICP	6.1	8.5	11.0	14.0
ZoomOut	6.1	8.7	7.5	15.0
SmoothShells	2.5	5.4	4.7	5.0
DiscreteOp	5.6	6.2	13.1	14.6
MWP	3.1	8.2	4.1	8.7
Unsupervised Methods				
Deep Shells	5.4	16.0	2.7	15.0
DUO-FMNet	4.2	4.4	2.7	3.1
WTFM	4.1	4.6	2.9	4.8
AttentiveFMaps	<u>2.6</u>	<u>2.8</u>	2.2	2.5
RFMNet	2.3	2.6	1.7	3.6
UnsupRSFMNet	6.7	8.9	4.8	7.0
Ours	2.7	2.9	<u>1.9</u>	<u>2.6</u>

Non-isometric shape matching. In the examination of non-isometric shape matching, our approach undergoes rigorous evaluation across two distinct datasets: SMAL_r [62] and DT4D-H [37]. The SMAL_r dataset is comprised of 49 shapes representing four-legged animals across eight species, partitioned into a training set of 29 instances and a testing set of 20 instances. On the other hand, DT4D-H encompasses nine classes of humanoid shapes, with a training-testing split of 198 and 95 instances, respectively. This bifurcated analysis serves to comprehensively assess the robustness and efficacy of our method in non-isometric shape-matching scenarios.

As shown in Table 3, our method exhibits superior performance compared to the existing state-of-the-art approaches on the challenging SMAL_r dataset. In the context of intra-class matching on the DT4D-H dataset, our method achieves perfect matching results. For inter-class shape matching, our approach surpasses existing axiomatic and unsupervised methods by a substantial margin, emerging as the top-performing method in this category when benchmarked against the current state-of-the-art. These findings underscore the effectiveness and versatility of our proposed method across diverse challenges in non-isometric shape matching. Fig. 4 illustrates some qualitative results of our method with comparisons to recent state-of-the-art methods on both SMAL_r [62] and DT4D-H [37] datasets. It observes that our method consistently outperforms existing

approaches, and produces smooth and accurate matching results even in the presence of large non-isometric distortions.

Table 3. Non-isometric matching on SMAL_r[62] and DT4D-H [37]. The numbers in the table are mean geodesic errors ($\times 100$). **Bold**: Best, Underline: Runner-up.

	SMAL _r	DT4D-H	
		intra-class	inter-class
Axiomatic Methods			
ZoomOut	38.4	4.0	29.0
SmoothShells	36.1	1.1	6.3
DiscreteOp	38.1	3.6	27.6
MWP	22.3	1.7	25.4
Unsupervised Methods			
Deep Shells	30.4	3.4	31.1
DUO-FMNet	32.8	2.6	15.8
WTFM	24.8	3.9	41.0
AttentiveFMaps	<u>5.4</u>	1.7	11.6
RFMNet	20.3	1.5	13.9
UnsupRSFMNet	7.1	<u>0.9</u>	<u>5.2</u>
Ours	4.3	0.9	4.2

Matching with topological noise. We further explored the case of topological changes in the areas of self-contact (e.g., touching hands generating a geodesic shortcut). For this task, we compare our method with the state of the art on the SHREC’16 Topology benchmark, which consists of 25 shape pairs (12K vertices) undergoing nearly isometric deformations with severe topological artifacts. As feature extractor DiffusionNet is not automatically robust to topological noise, we adopt a meaningful strategy from [22], which integrates input descriptor SHOT[49] and 7 residual multilayer perceptron (MLP) layers as the spatial feature extractors. The matching results are summarised in Table 4. Our method achieves the best matching performance and is much more robust against topological noise. Particularly, our method not only outperforms Deep Shells [14] by being more robust than intrinsic methods due to its basis in the spatial domain, but also surpasses RFMNet with the same feature extractor, which fully proves that our method is more effective. Meanwhile, a visual example is shown in Fig. 5 where our method provides smoother and more accurate color distribution than others.

6.4. Ablation study

The ablation studies we conduct on the challenging non-isometric dataset (e.g., SMAL_r [62]) aim to evaluate the importance of our three components, namely, the unsupervised loss in Section 5.3, the learning filter layer in Section 5.2, and the inference strategy in Section 5.4.

The results are summarized in Table 5. The first and second rows show the network trained without L_{freq} and L_{sm} , respectively. The third row indicates the spectral filter functions $H(\Lambda)$ obtained without updating their weight parameters. The fourth row represents the pointwise map

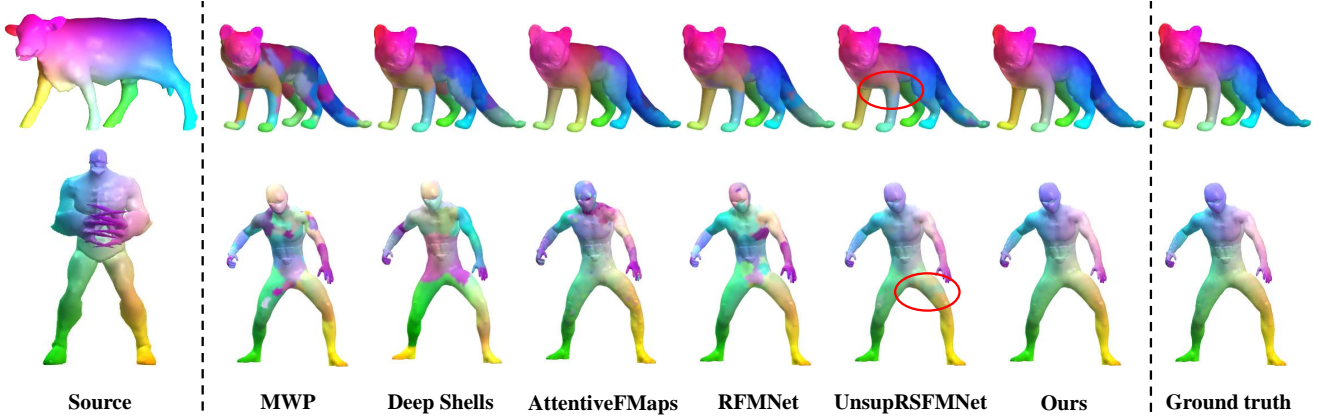


Figure 4. Comparisons with other methods on non-isometric shape matching. Correspondence is visualized by color transfer for shapes from the SMAL_r [62] (e.g. first row) and the DT4D-H datasets [37] (e.g. second row). Less error and color distortion happened in our method compared with the others, which shows our approach demonstrates superior matching performance for non-isometric shapes.

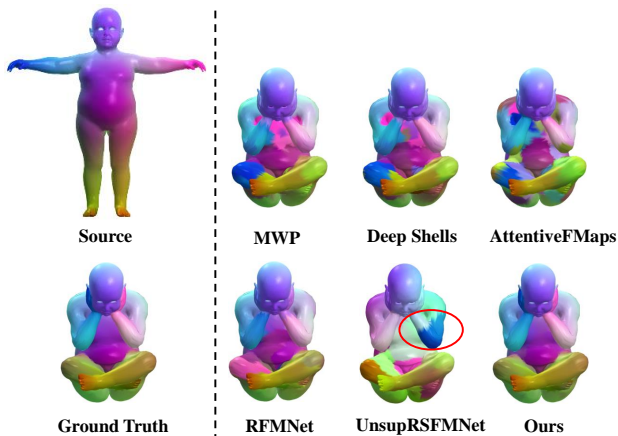


Figure 5. Comparisons with other methods on shape matching with topological noise, where shapes from SHREC’16 TOPKIDS benchmark [35]. The smoother and more accurate color distribution of our result illustrates our approach is more robust to topological noise compared to existing methods.

obtained at inference without using our inference strategy. By comparing the first row and the last row, we can conclude that L_{freq} indeed improves matching performance by a large margin. By comparing the second row and the last row, we observe that L_{sm} can improve the quantitative results. Comparing the third row and the last row shows that the learning filter layer plays an important role in accurate matching. Comparing the fourth row and the last row confirms that using our inference strategy yields better matching performance.

7. Discussion and Limitations

Although our constraint is induced from the isometric assumption, it explicitly models the functional maps, point-

Table 4. Topological noise on TOPKIDS[35]. The numbers in the table are mean geodesic errors ($\times 100$). **Bold**: Best, Underline: Runner-up.

TOPKIDS	
Axiomatic Methods	
ZoomOut	33.7
SmoothShells	11.8
DiscreteOp	35.5
MWP	5.7
Unsupervised Methods	
SURFMNet	48.6
Deep Shells	13.7
ConsistFMaps	39.3
WTFM	28.2
AttentiveFMaps	23.4
RFMNet	<u>4.9</u>
UnsupRSFMNet	23.8
Ours	3.3

Table 5. Ablation study on SMAL_r[62].

	SMAL _r
w.o L_{freq}	11.7
w.o L_{sm}	4.6
w.o learning filter layer	8.4
w.o our inference strategy	5.8
Ours	4.3

wise maps, and a set of filter functions. By using the proposed constraint as the loss function, as well as using extracted features compute both functional maps and pointwise maps, in a differentiable way during training, our approach thus ensures their simultaneous optimization and promotes their frequency awareness, resulting in not

only do the learned features thus extract accurate and robust shape features, but the data-driven filter functions encode significant and multi-resolution frequency information. Moreover, the optimized filter functions and extracted features are adequately adopted by our refinement strategy to compute the final correspondence during inference, leading to more accurate and robust matching results impulsively. Therefore, our approach can gracefully handle a range of matching scenarios, including non-isometric matching.

While our approach has achieved state-of-the-art performance in many challenging matching scenarios, it relies on the Polynomial Coefficient Decomposition technique (see Appendix B) to improve our generalization performance. Perhaps learning the filter representation by using orthonormal polynomials is not an optimal approach, as it would tend to introduce higher-order frequency information as well as trigger overfitting. So we might try to represent filter functions in terms of smooth and geometrically meaningful basis functions, like heat kernel, wavelet kernel, and others, which may be a direction worth exploring in the near future.

8. Conclusion

We introduce a novel general and powerful constraint to promote frequency awareness for functional map estimation. Based on this constraint, we develop a novel learning-based architecture for deformable shape matching by learning a set of filter functions. Our constraints not only can be utilized as the loss function to couple the functional maps, pointwise maps, and filter functions during the training stage, but also can be considered as an effective refinement strategy to refine the final pointwise map for more robust and accurate correspondences during inference. Extensive experimental results on different datasets demonstrate that our approach outperforms the existing state-of-the-art methods, especially in challenging settings such as non-isometric and inconsistent topology datasets.

Appendices

In this part, we first provide a proof in Appendix A for Remark 4.2. Next, we introduce more implementation details of using Jacobi basis to yield filter functions for our network in Appendix B. At last, we compare with UnsupRSFM-Net [6] by using the strategy of test-time-adaptation, and the quantitative results are summarized in Appendix C, Table 6.

A. Proofs of Remark 4.2

For convenience, we restate the remark as follows:

Remark A.1. *If the set of filter functions $\{h_s(\lambda)\}_{s=1}^S$ satisfy the Consistency Condition that $G(\lambda) = \sum_s h_s^2(\lambda) \neq$*

0, $\forall \lambda$, then the functional map $\mathbf{C}_{\mathcal{N}\mathcal{M}}$ in Eq.(8) can be obtained via

$$\mathbf{C}_{\mathcal{N}\mathcal{M}}^* = \left(\sum_s h_s(\Lambda_{\mathcal{M}}) \mathbf{C}_{\mathcal{N}\mathcal{M}}^{\Pi} h_s(\Lambda_{\mathcal{N}}) \right) (G^{-1}(\Lambda_{\mathcal{N}})),$$

where $G(\Lambda_{\mathcal{N}}) = \sum_s h_s^2(\Lambda_{\mathcal{N}})$.

Proof. Since the spectral filter operator is robust to isometric deformation, if the pointwise map $\Pi_{\mathcal{M}\mathcal{N}}$ also is an isometric map between shapes, we can obtain an analytic solution for $\mathbf{C}_{\mathcal{N}\mathcal{M}}$ via least square sense, the detailed derivation is given below:

$$\begin{aligned} \mathbf{C}_{\mathcal{N}\mathcal{M}} H(\Lambda_{\mathcal{N}}) &= H(\Lambda_{\mathcal{M}}) * \mathbf{C}_{\mathcal{N}\mathcal{M}}^{\Pi}, \\ \mathbf{C}_{\mathcal{N}\mathcal{M}} H(\Lambda_{\mathcal{N}}) H(\Lambda_{\mathcal{N}})^{\top} &= (H(\Lambda_{\mathcal{M}}) * \mathbf{C}_{\mathcal{N}\mathcal{M}}^{\Pi}) H(\Lambda_{\mathcal{N}})^{\top}, \\ \mathbf{C}_{\mathcal{N}\mathcal{M}} \sum_s h_s^2(\Lambda_{\mathcal{N}}) &= \sum_s h_s(\Lambda_{\mathcal{M}}) \mathbf{C}_{\mathcal{N}\mathcal{M}}^{\Pi} h_s(\Lambda_{\mathcal{N}}). \end{aligned}$$

As $G(\Lambda_{\mathcal{N}}) = \sum_s h_s^2(\Lambda_{\mathcal{N}}) \in \mathbb{R}^{k \times k}$ is a diagonal matrix, if it satisfies the condition

$$G(\lambda) = \sum_s h_s^2(\lambda) \neq 0, \forall \lambda, \quad (19)$$

the matrix $G(\Lambda_{\mathcal{N}})$ is invertible and computing its inverse is easy, and finally we have Eq.(9). \square

B. Jacobi Basis for Filter Functions

We will provide the details of Jacobi basis stated in Section 5.2 in the following. Among orthogonal polynomials, the Jacobi basis has a very general form, where some orthogonal bases are considered as its special cases, such as Chebyshev basis, Legendre basis, etc. The form of Jacobi basis $J_l^{a,b}$ can be expressed as

$$J_0^{a,b}(\lambda) = 1, J_1^{a,b}(\lambda) = \frac{a-b}{2} + \frac{a+b+2}{2}\lambda,$$

for $l \geq 2$.

$$J_l^{a,b}(\lambda) = (\mu_l \lambda + \mu'_l) J_{l-1}^{a,b}(\lambda) - \mu''_l J_{l-2}^{a,b}(\lambda),$$

where

$$\begin{aligned} \mu_l &= \frac{(2l+a+b)(2l+a+b-1)}{2l(l+a+b)}, \\ \mu'_l &= \frac{(2l+a+b-1)(a^2-b^2)}{2l(l+a+b)(2l+a+b-2)}, \\ \mu''_l &= \frac{(l+a-1)(l+b-1)(2l+a+b)}{l(l+a+b)(2l+a+b-2)}. \end{aligned}$$

$J_l^{a,b}$, $l = 0, 1, 2, \dots$ are orthogonal w.r.t. the weight function $(1-\lambda)^a (1+\lambda)^b$ on $[-1, 1]$. $J_l^{a,b}$ is Chebyshev basis when

Table 6. Evaluation on all datasets. The numbers in the table are mean geodesic errors ($\times 100$). **Bold**: Best. *TTA* denotes using Test-Time Adaptation from UnsupRFSMNet for refinement at inference time [6].

Train Test	F _r				S _r				SMAL _r	DT4T-H		TOPKIDS
	F _r	F _a	S _r	S _a	F _r	F _a	S _r	S _a		intra class	inter class	
UnsupRFSMNet	1.6	2.5	6.7	8.9	4.8	7.0	1.9	5.5	7.1	0.9	5.2	23.8
+TTA	1.6	1.9	2.2	2.4	1.6	2.1	1.9	1.9	3.9	0.9	4.1	9.1
Ours	1.6	2.0	2.7	2.9	1.9	2.6	1.9	1.9	4.3	0.9	4.2	3.3
+TTA	1.5	1.8	2.2	2.3	1.8	2.1	1.8	1.8	3.8	0.9	3.9	2.9

$a = b = \pm \frac{1}{2}$, and is Legendre basis when $a = b = 0$. Furthermore, according to [56], a and b can also be defined as learnable parameters in our Learning Filter layer, which could generate more proper a and b for Jacobi basis.

Since the Jacobi basis are defined in the interval $[-1, 1]$, the truncated eigenvalues Λ of the LBOs should be scaled to this interval accordingly. Thus, we rewrite the orthonormal Jacobi basis [56] as following:

$$\|J_l^{a,b}(\tilde{\lambda})\| = \sqrt{\frac{2^{a+b+1}\Gamma(l+a+1)\Gamma(l+b+1)}{(2l+a+b+1)\Gamma(l+a+b+1)l!}}$$

$$J_l(\tilde{\Lambda}) = \frac{J_l^{a,b}(\tilde{\Lambda})}{\|J_l^{a,b}(\tilde{\lambda})\|}.$$

where $\tilde{\Lambda} = \frac{2\Lambda}{\lambda_k} - \mathbf{I}_k$, $\mathbf{I}_k \in \mathbb{R}^{k \times k}$ is a identity matrix, and Γ is Gamma function. Then we have the learnable orthonormal Jacobi basis for yielding our filters, e.g.

$$h_s(\tilde{\Lambda}) = \sum_l w_{sl} J_l^{a,b}(\tilde{\Lambda}),$$

where $\{w_{sl}\}$ are trainable coefficients. In addition, in order to reduce the overfitting of our networks, we use the technique called Polynomial Coefficient Decomposition (PCD) [60] to decompose the polynomial coefficients. w_{sl} could be decomposed to $w_{sl} = \alpha_{sl} \prod_{i=0}^n \beta_i$, then we can modify the recursion formula to implement PCD.

$$J_l^{a,b}(\tilde{\Lambda}) = \beta_l(\mu_l \tilde{\Lambda} + \mu'_l) J_{l-1}^{a,b}(\tilde{\Lambda}) - \beta_l \beta_{l-1} \mu''_l J_{l-2}^{a,b}(\tilde{\Lambda}),$$

where $\beta_i = \beta' \tanh \gamma_i$, which enforces $\beta_i \in [-\beta', \beta']$.

C. Shape Matching with Test-Time Adaptation

For a fair comparison, we follow the refinement process of UnsupRFSMNet [6] and use test-time adaptation refinement to improve our performance. The matching results are summarised in Table 6. Note that our approach is superior to UnsupRFSMNet in most settings. Obviously, the results also show that the superior performance of UnsupRFSMNet heavily relies on the test-time adaptation process, our method is more robust than it.

References

- [1] Souhaib Attaiki, Gautam Pai, and Maks Ovsjanikov. Dpfm: Deep partial functional maps. In *International Conference on 3D Vision (3DV)*, pages 175–185. IEEE, 2021. 2, 3
- [2] Mathieu Aubry, Ulrich Schlickewei, and Daniel Cremers. The wave kernel signature: A quantum mechanical approach to shape analysis. In *2011 IEEE international conference on computer vision workshops (ICCV workshops)*, pages 1626–1633. IEEE, 2011. 4, 8
- [3] Mehmet Aygün, Zorah Löhner, and Daniel Cremers. Unsupervised Dense Shape Correspondence using Heat Kernels. In *International Conference on 3D Vision (3DV)*, pages 573–582, 2020. 3
- [4] F. Bogo, J. Romero, M. Loper, and M. J. Black. Faust: Dataset and evaluation for 3d mesh registration. In *IEEE Conference on Computer Vision and Pattern Recognition (CVPR)*, pages 3794–3801, 2014. 1
- [5] Dongliang Cao and Florian Bernard. Unsupervised Deep Multi-shape Matching. In *European Conference on Computer Vision – ECCV 2022*, pages 55–71, Cham, 2022. Springer Nature Switzerland. 3
- [6] Dongliang Cao, Paul Roetzer, and Florian Bernard. Unsupervised learning of robust spectral shape matching. *ACM Trans. Graph.*, 42(4), 2023. 1, 2, 3, 6, 7, 8, 11, 12
- [7] Luca Cosmo, Giorgia Minello, Michael Bronstein, Emanuele Rodolà, Luca Rossi, and Andrea Torsello. 3D Shape Analysis Through a Quantum Lens: the Average Mixing Kernel Signature. *International Journal of Computer Vision*, 130(6):1474–1493, 2022. 2
- [8] Marco Cuturi. Sinkhorn distances: Lightspeed computation of optimal transport. In *Advances in Neural Information Processing Systems (NeurIPS)*, 2013. 6
- [9] Nicolas Donati, Abhishek Sharma, and Maks Ovsjanikov. Deep geometric functional maps: Robust feature learning for shape correspondence. In *IEEE/CVF Conference on Computer Vision and Pattern Recognition (CVPR)*, pages 8589–8598, 2020. 2, 3
- [10] Nicolas Donati, Etienne Corman, Simone Melzi, and Maks Ovsjanikov. Complex Functional Maps: A Conformal Link Between Tangent Bundles. *Computer Graphics Forum*, 2022. 1, 2
- [11] Nicolas Donati, Etienne Corman, Simone Melzi, and Maks Ovsjanikov. Complex functional maps: A conformal link between tangent bundles. *Computer Graphics Forum*, 41(1): 317–334, 2022. 3

- [12] Nicolas Donati, Etienne Corman, and Maks Ovsjanikov. Deep orientation-aware functional maps: Tackling symmetry issues in shape matching. In *IEEE/CVF Conference on Computer Vision and Pattern Recognition (CVPR)*, pages 732–741, 2022. [3](#), [7](#), [8](#)
- [13] Marvin Eisenberger, Zorah Lahner, and Daniel Cremers. Smooth shells: Multi-scale shape registration with functional maps. In *Proceedings of the IEEE/CVF Conference on Computer Vision and Pattern Recognition*, pages 12265–12274, 2020. [1](#), [6](#), [7](#), [8](#)
- [14] Marvin Eisenberger, Aysim Toket, Laura Leal-Taixé, and Daniel Cremers. Deep shells: Unsupervised shape correspondence with optimal transport. *Advances in Neural Information Processing Systems*, 33:10491–10502, 2020. [7](#), [8](#), [9](#)
- [15] Marvin Eisenberger, David Novotny, Gael Kerchenbaum, Patrick Labatut, Natalia Neverova, Daniel Cremers, and Andrea Vedaldi. Neuromorph: Unsupervised shape interpolation and correspondence in one go. In *IEEE/CVF Conference on Computer Vision and Pattern Recognition (CVPR)*, pages 7469–7479, 2021. [1](#), [6](#)
- [16] Aoxiang Fan, Jiayi Ma, Xin Tian, Xiaoguang , and Wei Liu. Coherent point drift revisited for non-rigid shape matching and registration. In *IEEE/CVF Conference on Computer Vision and Pattern Recognition (CVPR)*, pages 1424–1434, 2022. [2](#)
- [17] Maolin Gao, Zorah Lahner, Johan Thunberg, Daniel Cremers, and Florian Bernard. Isometric multi-shape matching. In *Proceedings of the IEEE/CVF Conference on Computer Vision and Pattern Recognition (CVPR)*, pages 14183–14193, 2021. [2](#)
- [18] Oshri Halimi, Or Litany, Emanuele Rodolà Rodolà, Alex M. Bronstein, and Ron Kimmel. Unsupervised learning of dense shape correspondence. In *IEEE/CVF Conference on Computer Vision and Pattern Recognition (CVPR)*, pages 4365–4374, 2019. [2](#), [3](#)
- [19] David K Hammond, Pierre Vandergheynst, and Remi Gribonval. Wavelets on graphs via spectral graph theory. *Applied and Computational Harmonic Analysis*, 30(2):129–150, 2011. [6](#)
- [20] Florine Hartwig, Josua Sassen, Omri Azencot, Martin Rumpf, and Mirela Ben-Chen. An elastic basis for spectral shape correspondence. In *ACM SIGGRAPH 2023 Conference Proceedings*, New York, NY, USA, 2023. Association for Computing Machinery. [1](#), [2](#)
- [21] Ling Hu, Qinsong Li, Shengjun Liu, and Xinru Liu. Efficient deformable shape correspondence via multiscale spectral manifold wavelets preservation. In *IEEE/CVF Conference on Computer Vision and Pattern Recognition (CVPR)*, pages 14531–14540, 2021. [1](#), [2](#), [3](#), [4](#), [5](#), [6](#), [7](#), [8](#)
- [22] Ling Hu, Qinsong Li, Shengjun Liu, Dong-Ming Yan, Haojun Xu, and Xinru Liu. Rfmnet: Robust deep functional maps for unsupervised non-rigid shape correspondence. *Graphical Models*, 129:101189, 2023. [2](#), [3](#), [7](#), [8](#), [9](#)
- [23] Qixing Huang, Fan Wang, and Leonidas Guibas. Functional map networks for analyzing and exploring large shape collections. *ACM Trans. Graph.*, 33(4), 2014. [2](#)
- [24] Ruqi Huang, Jing Ren, Peter Wonka, and Maks Ovsjanikov. Consistent zoomout: Efficient spectral map synchronization. *Computer Graphics Forum*, 39(5):265–278, 2020. [2](#)
- [25] Vladimir G. Kim, Yaron Lipman, and Thomas Funkhouser. Blended intrinsic maps. *ACM Trans. Graph.*, 30(4), 2011. [8](#)
- [26] Diederik P Kingma and Jimmy Ba. Adam: A method for stochastic optimization. In *International Conference for Learning Representations (ICLR)*, 2015. [8](#)
- [27] Nora Leonardi and Dimitri Van De Ville. Tight wavelet frames on multislice graphs. *IEEE Transactions on Signal Processing*, 61(13):3357–3367, 2013. [5](#)
- [28] Lei Li, Nicolas Donati, and Maks Ovsjanikov. Learning multi-resolution functional maps with spectral attention for robust shape matching. *Advances in Neural Information Processing Systems*, 35:29336–29349, 2022. [3](#), [8](#)
- [29] Qinsong Li, Ling Hu, Shengjun Liu, Dangfu Yang, and Xinru Liu. Anisotropic Spectral Manifold Wavelet Descriptor. *Computer Graphics Forum*, 40(1):81–96, 2021. [2](#)
- [30] Or Litany, Tal Remez, Emanuele Rodolà, Alex Bronstein, and Michael Bronstein. Deep functional maps: Structured prediction for dense shape correspondence. In *IEEE International Conference on Computer Vision (ICCV)*, pages 5660–5668, 2017. [2](#)
- [31] O. Litany, E. Rodolà, A. M. Bronstein, and M. M. Bronstein. Fully Spectral Partial Shape Matching. *Computer Graphics Forum*, 36(2):247–258, 2017. [1](#), [2](#)
- [32] Shengjun Liu, Haojun Xu, Dong ming Yan, Ling Hu, Xinru Liu, and Qinsong Li. Wtfm layer: An effective map extractor for unsupervised shape correspondence. *Computer Graphics Forum*, 2022. [2](#)
- [33] Shengjun Liu, Haojun Xu, Dong-Ming Yan, Ling Hu, Xinru Liu, and Qinsong Li. Wtfm layer: An effective map extractor for unsupervised shape correspondence. In *Computer Graphics Forum*, pages 51–61. Wiley Online Library, 2022. [8](#)
- [34] Shengjun Liu, Feifan Luo, Qinsong Li, Xinru Liu, and Ling Hu. Awedd: a descriptor simultaneously encoding multiscale extrinsic and intrinsic shape features. *The Visual Computer*, 2023. [2](#)
- [35] Z. Löhner, E. Rodolà, M. M. Bronstein, D. Cremers, O. Burghard, L. Cosmo, A. Dieckmann, R. Klein, and Y. Sahillioglu. Matching of Deformable Shapes with Topological Noise. In *Eurographics Workshop on 3D Object Retrieval*. The Eurographics Association, 2016. [10](#)
- [36] Robin Magnet, Jing Ren, Olga Sorkine-Hornung, and Maks Ovsjanikov. Smooth non-rigid shape matching via effective dirichlet energy optimization. In *2022 International Conference on 3D Vision (3DV)*, pages 495–504, 2022. [1](#), [2](#)
- [37] Robin Magnet, Jing Ren, Olga Sorkine-Hornung, and Maks Ovsjanikov. Smooth Non-Rigid Shape Matching via Effective Dirichlet Energy Optimization. In *2022 International Conference on 3D Vision (3DV)*, pages 495–504, Prague, Czech Republic, 2022. IEEE. [9](#), [10](#)
- [38] S. Melzi, R. Marin, E. Rodolà, U. Castellani, J. Ren, A. Poulernard, P. Wonka, and M. Ovsjanikov. Matching Humans with Different Connectivity. In *Eurographics Workshop on 3D Object Retrieval*. The Eurographics Association, 2019. [1](#), [2](#), [8](#)

- [39] Mark Meyer, Mathieu Desbrun, Peter Schröder, and Alan H Barr. Discrete differential-geometry operators for triangulated 2-manifolds. In *Visualization and mathematics III*, pages 35–57. Springer, 2003. 3
- [40] Dorian Nogneng and Maks Ovsjanikov. Informative descriptor preservation via commutativity for shape matching. *Computer Graphics Forum*, 36(2):259–267, 2017. 1, 2
- [41] Maks Ovsjanikov, Mirela Ben-Chen, Justin Solomon, Adrian Butscher, and Leonidas Guibas. Functional maps: A flexible representation of maps between shapes. *ACM Trans. Graph.*, 31(4), 2012. 1, 2, 5
- [42] Jing Ren, Adrien Poulenard, Peter Wonka, and Maks Ovsjanikov. Continuous and orientation-preserving correspondences via functional maps. *ACM Transactions on Graphics (ToG)*, 37(6):1–16, 2018. 2, 8
- [43] Jing Ren, Mikhail Panine, Peter Wonka, and Maks Ovsjanikov. Structured Regularization of Functional Map Computations. *Computer Graphics Forum*, 38(5):39–53, 2019. 2, 4, 5, 6, 7, 8
- [44] Jing Ren, Simone Melzi, Peter Wonka, and Maks Ovsjanikov. Discrete optimization for shape matching. *Computer Graphics Forum*, 40(5):81–96, 2021. 2, 8
- [45] Jing Ren, Simone Melzi, Peter Wonka, and Maks Ovsjanikov. Discrete optimization for shape matching. In *Computer Graphics Forum*, pages 81–96. Wiley Online Library, 2021. 4
- [46] E. Rodolà, L. Cosmo, M. M. Bronstein, A. Torsello, and D. Cremers. Partial Functional Correspondence. *Computer Graphics Forum*, 36(1):222–236, 2017. 1, 2
- [47] Jean-Michel Roufousse, Abhishek Sharma, and Maks Ovsjanikov. Unsupervised deep learning for structured shape matching. In *IEEE/CVF International Conference on Computer Vision (ICCV)*, pages 1617–1627, 2019. 2, 3
- [48] Yusuf Sahillioğlu. Recent advances in shape correspondence. *The Visual Computer*, 36(8):1705–1721, 2020. 2
- [49] Samuele Salti, Federico Tombari, and Luigi Di Stefano. Shot: Unique signatures of histograms for surface and texture description. *Computer Vision and Image Understanding*, 125:251–264, 2014. 2, 9
- [50] Abhishek Sharma and Maks Ovsjanikov. Weakly supervised deep functional maps for shape matching. In *Advances in Neural Information Processing Systems (NeurIPS)*, 2020. 2, 3
- [51] Nicholas Sharp, Souhaib Attaiki, Keenan Crane, and Maks Ovsjanikov. Diffusionnet: Discretization agnostic learning on surfaces. *ACM Trans. Graph.*, 41(3), 2022. 2, 3
- [52] Robert W. Sumner and Jovan Popović. Deformation transfer for triangle meshes. *ACM Trans. Graph.*, 23(3):399–405, 2004. 1
- [53] Jian Sun, Maks Ovsjanikov, and Leonidas Guibas. A concise and provably informative multi-scale signature based on heat diffusion. In *Computer graphics forum*, pages 1383–1392. Wiley Online Library, 2009. 4
- [54] Jian Sun, Maks Ovsjanikov, and Leonidas Guibas. A concise and provably informative multi-scale signature based on heat diffusion. *Computer Graphics Forum*, 28(5):1383–1392, 2010. 2
- [55] Mingze Sun, Shiwei Mao, Puhua Jiang, Maks Ovsjanikov, and Ruqi Huang. Spatially and spectrally consistent deep functional maps. In *Proceedings of the IEEE/CVF International Conference on Computer Vision (ICCV)*, pages 14497–14507, 2023. 2, 3
- [56] Qian Tao, Zhen Wang, Wenyuan Yu, Yaliang Li, and Zhewei Wei. Longnn: Spectral gnns with learnable orthonormal basis. *arXiv preprint arXiv:2303.13750*, 2023. 12
- [57] Hugues Thomas, Charles R. Qi, Jean-Emmanuel Deschaud, Beatriz Marcotegui, François Goulette, and Leonidas Guibas. Kpconv: Flexible and deformable convolution for point clouds. In *IEEE/CVF International Conference on Computer Vision (ICCV)*, pages 6410–6419, 2019. 3
- [58] Matthias Vestner, Zorah Löhner, Amit Boyarski, Or Litany, Ron Slossberg, Tal Remez, Emanuele Rodola, Alex Bronstein, Michael Bronstein, Ron Kimmel, et al. Efficient deformable shape correspondence via kernel matching. In *2017 international conference on 3D vision (3DV)*, pages 517–526. IEEE, 2017. 2, 4, 5, 6
- [59] Matthias Vestner, Roe Litman, Emanuele Rodola, Alex Bronstein, and Daniel Cremers. Product manifold filter: Non-rigid shape correspondence via kernel density estimation in the product space. In *Proceedings of the IEEE Conference on Computer Vision and Pattern Recognition (CVPR)*, pages 3327–3336, 2017. 2
- [60] Xiyuan Wang and Muhan Zhang. How powerful are spectral graph neural networks. In *International Conference on Machine Learning*, pages 23341–23362. PMLR, 2022. 12
- [61] Rui Xiang, Rongjie Lai, and Hongkai Zhao. Efficient and robust shape correspondence via sparsity-enforced quadratic assignment. In *Proceedings of the IEEE/CVF Conference on Computer Vision and Pattern Recognition (CVPR)*, pages 9513–9522, 2020. 2
- [62] Silvia Zuffi, Angjoo Kanazawa, David W Jacobs, and Michael J Black. 3d menagerie: Modeling the 3d shape and pose of animals. In *Proceedings of the IEEE conference on computer vision and pattern recognition*, pages 6365–6373, 2017. 9, 10